



Cite this: *Phys. Chem. Chem. Phys.*,
2022, 24, 14072

Ultrafast CO₂ photodissociation in the energy region of the lowest Rydberg series

Johan F. Triana, ^a Daniel Peláez, ^b Majdi Hochlaf ^c and
José L. Sanz-Vicario ^{†*d}

We present a detailed theoretical survey of the electronic structure of excited states of the CO₂ molecule, with the aim of providing a well-defined theoretical framework for the quantum dynamical studies at energies beyond 12 eV from the ground state. One of the major goals of our work is to emphasize the need for dealing with the presence of both molecular valence and Rydberg states. Although a CASSCF/MRCI approach can be used to appropriately describe the lowest-lying valence states, it becomes incapable of describing the upper electronic states due to the exceedingly large number of electronic excitations required. To circumvent this we employ instead the EOM-CCSD monoconfigurational method to describe the manifold of both valence and Rydberg states in the Franck–Condon region and then a matching procedure to connect these EOM-CCSD eigensolutions with those obtained from CASSCF/MRCI in the outer region, thus ensuring the correct asymptotic behavior. Within this hybrid level of theory, we then analyze the role of valence and Rydberg states in the dynamical mechanism of the photodissociation of quasi-linear CO₂ into CO + O fragments, by considering a simple but effective 1D multistate non-adiabatic model for the ultrafast C–O bond break up. We show evidence that the metastability of the Rydberg states must be accounted for in the ultrafast dynamics since they produce changes in the photodissociation yields within the first tens of fs.

Received 1st March 2022,
Accepted 29th April 2022

DOI: 10.1039/d2cp01017h

rsc.li/pccp

1 Introduction

The CO₂ molecule is of paramount importance in atmospheric physics, living bodies and quite important as industrial materials, involved in a huge variety of domains ranging from atmospheric chemistry, biological systems and industrial processes. Carbon dioxide has become a well-known worldwide molecule associated with the greenhouse effect leading to global warming, since this molecule also intervenes in the combustion of fossil fuels, and its excess is not alleviated by the forest cover due to continuous deforestation. Due to the ubiquitous presence of this molecule in open air, the study of its photochemical processes becomes significant.

Interestingly, in spite of being a simple triatomic molecule, the structure and photodynamics have not been entirely

resolved for CO₂ in the VUV photon range. This work is motivated by the very challenging experiments of state-to-state photodissociation of the CO₂ molecule in the VUV domain performed in the recent years by the groups at Davis¹ and at Dalian.^{2,3} Lu *et al.*,¹ presented a state-to-state photodissociation study of CO₂ in the VUV range (11.94–12.20 eV) using the velocity map imaging photoion (VMI-PI) method along with the state of the art molecular electronic structure calculations for the relevant potential energy surfaces (PESs). In that work, two main spin-allowed fragmentation pathways were detected in this VUV region, namely, CO(X¹Σ⁺; ν = 0–18) + O(¹D) and CO(X¹Σ⁺; ν = 0–9) + O(¹S), vibrationally-resolved for the carbon monoxide (note that dissociation is faster than the rotation periods of CO₂). A simple static analysis of the molecular PESs seems to indicate that the former dissociation channel is entirely due to the population of the 4¹A' state in the Franck–Condon (FC) region, which subsequently dissociates straightforwardly due to its repulsive character and the absence of relevant topographical features along the path. However, the latter dissociation proceeds instead by a non-adiabatic transition from the initially populated 4¹A' state to the lower 3¹A' state through the seam of a conical intersection. Although this explanation is plausible within the picture provided by purely valence states, the electronic structure of the CO₂ molecule at this energy is more complicated due to the ubiquitous presence

^a Department of Physics, Universidad de Santiago de Chile, Av. Víctor Jara 3493, Estación Central, Chile. E-mail: johan.triana@usach.cl

^b Institut des Sciences Moléculaires d'Orsay (ISMO), Université Paris-Saclay, Orsay, France. E-mail: daniel.pelaez-ruiz@universite-paris-saclay.fr

^c Université Gustave Eiffel, COSYS/LISIS, 5 Bd Descartes 77454, Champs-sur-Marne, France. E-mail: majdi.hochlaf@univ-eiffel.fr

^d Grupo de Física Atómica y Molecular, Instituto de Física, Universidad de Antioquia, Medellín, Colombia. E-mail: jose.sanz@udea.edu.co

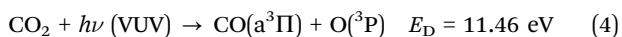
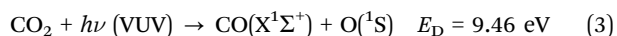
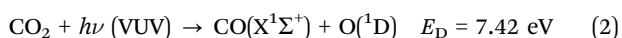
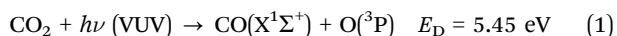
[†] Present address: Departamento de Química-Física. Facultad de Ciencias Químicas. Universidad Complutense de Madrid. Spain. E-mail: josanz11@ucm.es

of Rydberg molecular states in the FC region, also in this 11.94–12.20 eV VUV photon range, as it will be subsequently shown. In the previous work Rydberg states were not considered in the accompanying theoretical computations and our contribution here gives caveats since this $4^1A' \rightarrow 3^1A'$ mechanism is widely cited now.^{2–4}

Accurate and comprehensive electronic structure computations of the CO₂ molecule using CASSCF, MRCI and EOM-CCSD methods have been championed by Grebenshchikov with the analysis of the multidimensional potential energy surfaces (PESs) for the lowest states^{5–7} but also for superexcited states,⁸ thus announcing the complex landscape to be considered when carrying out photodynamical studies in CO₂.

Our proposal here is to revisit CO₂ but incorporating a fuller scheme with both valence and Rydberg states, not only from a static perspective but also by studying the involved photodynamics in the time domain and investigating the dynamical implications of their presence. The importance of including Rydberg states is twofold; first, A' Rydberg states are already present between the previously reported $3^1A'$ and $4^1A'$ valence states. We find in this study that some of the ripples and barriers present in the reported PESs in Lu *et al.*¹ of these valence states consist of artifacts due to the neglect of including explicitly Rydberg orbitals in the active space (appropriately represented with diffuse basis sets) with the ability to generate Rydberg states in a variational calculation. Secondly, transitions to Rydberg states are also spin-allowed in the Franck–Condon region in this VUV range. Thus their role in the full photodynamics must be gauged with the explicit calculation of their energies, oscillator strengths, lifetimes and their coupling with the closely lying valence states.

It is known that noticeable CO₂ absorption bands begin to appear from 6.2 eV photons but the main photodissociation processes are expected to occur at $h\nu$ (VUV) > 11.0 eV. Different photoproduct channels of CO₂ accessible with VUV excitation within the singlet excitation manifold have already been reported (see for instance¹)



where we quote the fragmentation threshold energies E_{D} from the ground state. Other detected CO + O photofragment channels in the ~13 eV photon energy region are CO($\text{a}^3\Sigma^+$) + O(P), CO($\text{d}^3\Delta$) + O(P), CO($\text{e}^3\Sigma^-$) + O(P) and CO($\text{a}^3\Pi$) + O(D)⁹ and higher up in excitation energy the dissociation into molecular oxygen has been also observed [C(P) + O₂ ($\text{X}^3\Sigma^-_g$)] for photon energies $h\nu = 11.5$ – 12.2 eV.¹⁰ All this highlights the profusion of fragmentation channels above $h\nu = 11.0$ eV.

On the theoretical side, it is challenging to predict branching ratios for this plethora of photodissociation channels. To our knowledge, the most detailed theoretical studies of excited states in CO₂ have been carried out by Buenker *et al.*¹¹ and

more recently and comprehensively by Grebenshchikov.^{5–8} Buenker *et al.* performed a theoretical study of excited states by the multireference single and double excitation configuration interaction method (MRD-CI). They explored both linear and bent geometries of CO₂, for vertical and non-vertical transitions, since some excited states are more stable in bent geometries. In this respect they computed energies for CO₂ considering $D_{\infty h}$ and C_{2v} point groups. Grebenshchikov produced the global PESs for the lowest three states of both $^1A'$ and $^1A''$ symmetries in the C_s point group. This systematic *ab initio* study of singlet PESs with three internal coordinates (R_1 , R_2 , θ) using the MRCI level of theory requires a considerable computational effort (note that the author only reports 3 states per symmetry in the C_s point group). This latter work represents an accurate computation of energies and molecular properties for linear and bent geometries, and also to describe the presence and characterization of some conical intersections, whose presence makes the dynamical computations rather complicated. Also, Grebenshchikov and coworkers⁸ ventured into the computation of superexcited states of CO₂ in the FC region using the equation of motion coupled-cluster singles and doubles (EOM-CCSD) method,¹² uncovering a large number of intermingled Rydberg states. These latter works are very detailed concerning the electronic structure and our intention is not to improve on that.

However, for CO + O fragmentation, considering the previous works (Lu *et al.*¹ showed that CO₂ remains close to a linear geometry before dissociating at this excitation energy), a good approximation is to assume a reduced dimensionality, by taking vertical transitions in the FC region and dissociation along a single bond distance C–O. With this approximation, our purpose is to explore a larger number of valence and Rydberg states by moving from the MCSCF/MRCI method (for which the computational cost becomes prohibitive for high excitations) to the EOM-CCSD method, which is much less expensive computationally. It provides more reasonable results for vertical excitation energies within the FC region. Nevertheless, owing to its single-determinant reference wave function, EOM-CCSD fails to reproduce the correct dissociation energies in the fragmentation channels. Therefore we smoothly connect the EOM energies of Rydberg states with those of the MRCI valence states that eventually leads to dissociation. We then proceed with a diabaticization procedure that allows us to carry out photodynamical calculations within this 1D reduced model. Our photodissociation calculations are based on *ab initio* nuclear wavepacket (WP) dynamics with a grid-based DVR method using the multi-configurational time dependent Hartree (MCTDH) code.¹³ We report the atomistic inner workings of CO₂ photofragmentation within the first stage, in the femtoseconds ultrafast time window, where some features can be unambiguously attributed to the participation of Rydberg states.

This work is divided into two major parts: our electronic structure calculations are first described in section 2 and our steps to calculate multistate non-adiabatic photodissociation yields using ultrashort laser pulses are included in section 3. We end up with some concluding remarks.

2 Electronic structure calculations

We have performed all *ab initio* calculations using the MOLPRO molecular package (version 2015).¹⁴ Since Abelian continuous groups are not implemented in this package, we have considered to compute CO₂ within the *C_s* point group, which contains the two irreducible representations (IR) *A'* and *A''*.

All our calculations are performed by setting the molecule along the *z*-axis with the carbon atom in the coordinate origin, and the molecular plane is *yz* for bent CO₂ geometries. In order to compare with the calculations by Buenker *et al.*¹¹ quoted as computed using the *C_{2v}* point group, our plane σ (*y, z*) reduces to the molecular plane σ in the *C_s* point group, thus with the following correlations for the IRs: *A₁*, *A₂*, *B₁* and *B₂* in *C_{2v}* correspond to *A'*, *A''*, *A''* and *A'* in *C_s*, respectively.¹⁵ Similarly, IRs in *D_{∞h}* can be also correlated to those of lower symmetry in *C_{2v}*, by making our *y*-axis to act as the *C₂* axis (*z* → *y* case in Table 59, Appendix 4 in the book by Herzberg¹⁵). The latter is the same correlation used by Buenker *et al.*¹¹

We have computed optimized molecular orbitals for CO₂ at the CASSCF level of theory with different basis (see below). With this set of optimized MOs at the equilibrium geometry of the electronic ground state we can organize the diagram of molecular orbitals generated from the atomic orbitals in C and O. Following the energy ordering for the occupied MO, the simplified SCF-HF electronic configuration of CO₂ can be described according to the two different point groups *D_{∞h}* and *C_s*, namely,

- $[1\sigma_g^2 1\sigma_u^2 2\sigma_g^2] 3\sigma_g^2 2\sigma_u^2 4\sigma_g^2 3\sigma_u^2 1\pi_u^4 1\pi_g^4$ in *D_{∞h}*.
- $[1a'^2 2a'^2 3a'^2] 4a'^2 5a'^2 6a'^2 7a'^2 8a'^2 1a''^2 9a''^2 2a''^2$ in *C_s*.

where the brackets enclose inner core orbitals. In the present work we are interested only in spin-allowed transitions from the singlet ground state *X*¹*A'* and therefore we will refer to spin singlets excited states.

Excited states can be understood in terms of leading electron excitations from HOMO−*n* to LUMO+*m*, the lowest excitations coming from the degenerate HOMO 9*a'* and 2*a''* to the LUMO+*m*, with *m* = 0,1,2,... In molecules it is important to realize that many MOs that mostly remain with an atomic character may stabilize energetically below the valence MOs formed from occupied AOs in C and O. For instance, the MO 10*a'* preserves the 3*s* atomic nature and it relaxes energetically to become the LUMO in CO₂. The lowest HOMO–LUMO excitations 9*a'* → 10*a'* and 2*a''* → 10*a'* thus represent the main components for the lowest excited states {2¹*A'*, 1¹*A''*}, respectively. It means that these two lowest states already show a Rydberg mixed component. This is not the exception but the rule; whereas the next three excited states 2¹*A''* and {3¹*A'*, 3¹*A''*} (the latter two energy degenerated) correspond to transitions from the valence HOMO to valence unoccupied MO {16*a'*, 6*a''*}, the rest of the excited states between 11 and 12.5 eV have a Rydberg excitation character at the equilibrium geometry. To disclose that this series of Rydberg states strongly depends on the type of basis used in the computation. We identify the

Rydberg orbitals by inspection after the MCSCF calculation, being characterized as very diffuse orbitals with an atomic character centered on the C atom. In this respect, the work by Spielfiedel *et al.*¹⁶ called for attention to the interaction between valence and Rydberg states in CO₂. They identified the presence of avoided crossings between valence and Rydberg states. To achieve those results, the regular basis of Huzinaga and Dunning^{17,18} had to be enlarged with diffuse *s*, *p* and *d* functions for both C and O. In the present work to produce Rydberg orbitals we have used the ANO-L basis (atomic natural orbitals, large) of Roos *et al.*¹⁹ as implemented in MOLPRO, also enlarged with *s*, *p* and *d* functions over the C atom.

As a result Spielfiedel *et al.* identified four Rydberg orbitals 2*π_g*, 4*σ_u*, 3*π_u*, and 1*δ_g* in the *D_{∞h}* point group, which must correspond to our four sets of Rydberg orbitals {11*a'*, 3*a''*}, 12*a'*, {13*a'*, 4*a''*} and {14*a'*, 5*a''*} included in Fig. 1 (middle panel). In addition we also find the Rydberg orbitals 10*a'* (3*s*) and 15*a'* (3*d_σ*). The valence orbital 2*π_u* quoted in ref. 16 must be our valence orbitals {16*a'*, 6*a''*} and their 5*σ_g* corresponds to our orbital 17*a'*.

We enforce the *C_s* symmetry in MOLPRO calculations we define the bond angle $\theta = 179.99^\circ$. A lower symmetry *C_s* allows the flexibility to represent CO₂ with different bond angles and bond distances at the same time. Our first step was to compare our results with the previous computations included in Lu *et al.*,¹ for the four lowest roots of ¹*A'* symmetry (including the ground state) and lowest three excited states of ¹*A''* symmetry, and we present here two types of calculations for a 1D reduced dimensionality (one of the bond distances is kept fixed at *R*₁ = 2.2 bohr and the other is varied 1.7 ≤ *R*₂ ≤ 7 bohr). For the PECs shown in this work we use a grid of distances *R*_{CO} with $\Delta R = 0.1$ for *R*_{CO} ∈ [1.7,3.4] bohr, $\Delta R = 0.2$ for *R*_{CO} ∈ [3.8,5.0] bohr and $\Delta R = 0.5$ for *R*_{CO} ∈ [5.0,7.0] bohr. In these preliminary calculations, we stress that only the three lowest excited states of *A'* and *A''* symmetry are calculated as roots in the MCSCF/MRCI procedure.

The first type of calculation is almost identical to that performed by Lu *et al.*¹ We use a generally contracted aug-cc-pV5Z basis set by Dunning *et al.*^{17,18,20,21} to describe the orbitals of the three atoms. This consists of 381 contracted Gaussian type functions. Energies are obtained using the complete active space self-consistent field (CASSCF)^{22,23} method, followed by the internally contracted MRCI approach.^{24,25} In CASSCF calculations, the lowest three *a'* orbitals (1*a'*, 2*a'*, 3*a'*) were optimized but kept doubly occupied in a core. Then, we use twelve valence orbitals (nine *a'* and three *a''*) in the active space for sixteen fully correlated valence electrons, which amounts to more than 3.5 × 10⁴ configurations state functions (CSFs) in each IR of the *C_s* point group. Also, the electronic states with the same spin multiplicity are averaged together using the procedure implemented in the MOLPRO program.¹⁴ For MRCI calculations, those configurations with a weight ≥ 0.05 in the CI expansion of the CASSCF wave functions act as a reference. This leads to more than 1.6 × 10⁸ (2 × 10⁷) uncontracted (contracted) CSFs to be considered per *C_s* symmetry for the singlets. We call this type of calculations full valence active space with sixteen electrons in twelve valence orbitals, FVAS (16,12).

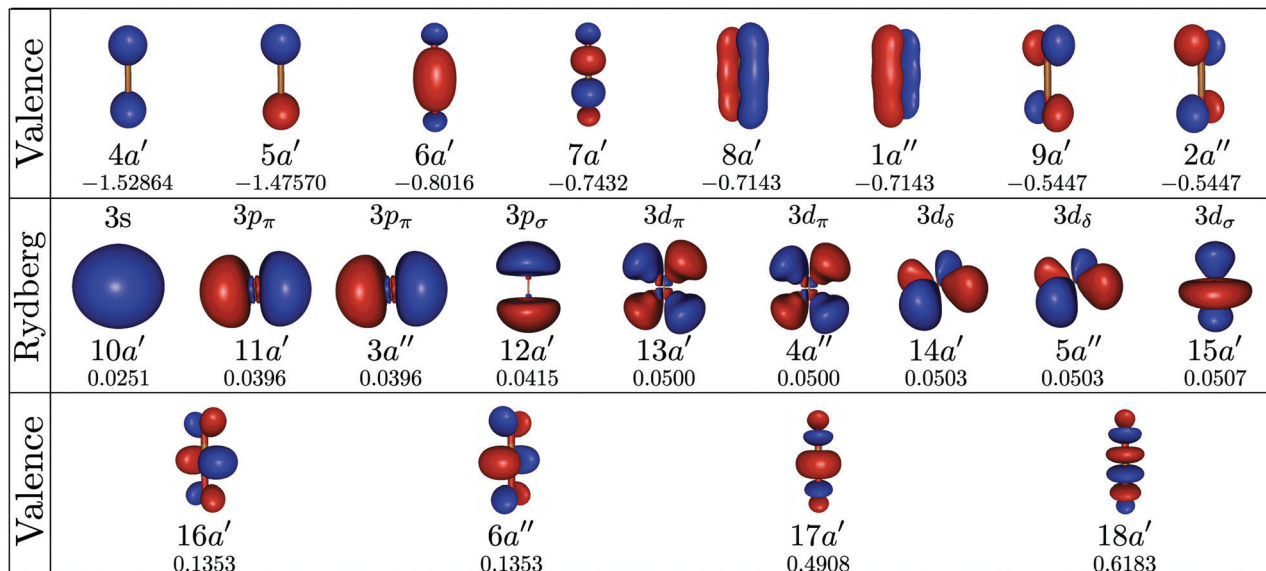


Fig. 1 Plots of energy-ordered molecular orbitals in the CO₂ molecule as optimized using an MCSCF procedure with their corresponding orbital energies at the equilibrium geometry of CO₂ in its ground electronic state. Top panel: occupied valence MO outside the core [1a'2a'3a'] with degenerate HOMO 9a' and 2a'' (π_g); Middle panel: unoccupied MO with a Rydberg character, including degeneracies {11a', 3a''} (3p_π), {13a', 4a''} (3d_π) and {14a', 5a''} (3d_δ); Bottom panel: highly excited unoccupied valence orbitals, with degeneracy {16a', 6a''} (π_u). MO energies are included below the MO labels. By inspection it is easy to correlate these orbitals to the IR in D_{∞h} point group. Relative sizes have been adapted in order to fit in the figure.

The second type of calculation was carried out using an ANO-L basis set¹⁹ plus diffuse s, p and d type functions located at the carbon atom,²⁶ in order to better describe the low-lying 10a' (3s) Rydberg MO of CO₂. Like above, these states were computed using the CASSCF method, followed by the internally contracted MRCI approach. Here, in our CASSCF calculations, the five lowest a' orbitals were optimized but kept doubly occupied and there are eleven orbitals (seven a', three a'') plus the diffuse Rydberg orbital 10a' in the active space (see Fig. 1) for twelve correlated electrons. This results in more than 2.1×10^4 CSFs to be considered in each symmetry of the C_s point group for the singlets. For MRCI calculations, all configurations having a weight ≥ 0.02 in the CI expansion of the CASSCF wavefunctions were taken into account as a reference. This leads to more than 1.5×10^8 (7.6×10^6) uncontracted (contracted) CSFs to be considered per C_s symmetry (spin singlets). In conclusion, we reduce the number of valence orbitals but we additionally include a Rydberg orbital in the active space, 10a'(3s), which is the main orbital responsible for the excitation that corresponds to the states 2¹A' and (see ref. 11 and Table 1). We call this calculation partial valence active space with twelve electrons in eleven active orbitals, *i.e.*, PVAS (12,11).

Fig. 2 shows the comparison between the potential energy curves obtained with these two different types of calculations. First, it must be noted again that the adiabatic energies obtained with FVAS (16,12) are computed using only valence orbitals (from Fig. 1, all states 1–4 ¹A' and 1–3 ¹A'' in the figures are the lowest roots and they can be named pure valence states). These states correspond to those already plotted in Fig. 11 of Lu *et al.*¹ In Fig. 2 we also include our results using the PVAS (12,11) calculation. Four features in the energy curves

are noteworthy: (i) the states 3¹A' and 2¹A'' calculated with FVAS (16,12) display a twist located at $R \sim 2.4$ bohr that vanishes with the PVAS (12,11) calculation, (ii) the 4¹A' state computed with FVAS shows a smooth energy variation at small internuclear distances at variance with the PVAS, with a strong oscillatory behavior, (iii) a conical intersection between the 3¹A' and the 4¹A' states at $R \sim 3.6$ bohr and (iv) a low potential barrier in the 4¹A' state leading to the CO(X¹Σ⁺) + O(¹S) fragmentation channel.

From our results concerning item (i) we can conclude that the wiggle at $R \sim 2.4$ bohr is a spurious effect due to the lack of diffuse Rydberg orbitals in the active space chosen for the FVAS calculation. As discussed below, the lowest excited states 2¹A' and 1¹A'' are already represented by leading excitations from the HOMO to the LUMO 10a' (lowest Rydberg 3s orbital). Even with a smaller active space, the PVAS calculation that introduces a single Rydberg orbital is able to relax the electronic energy. Nevertheless, FVAS calculations can reproduce well these two lowest Rydberg states, but at the cost of misrepresenting the upper states 3¹A' and 3¹A'', which are valence states indeed. In short, the introduction of orbitals with a diffuse Rydberg character in the active space, unveils the presence of several mixed valence-Rydberg states as well as improves the energies of valence states. With respect to item (ii), it is precisely because of the introduction of Rydberg orbitals that the PVAS method tries to variationally relax the electronic energies to the undisclosed Rydberg states lying below the 4¹A' at short distances, within the FC region, *i.e.*, these oscillations represent an indication of the presence of electronic states between the 3¹A' and the 4¹A' valence states. So to say, the exclusive use of valence orbitals (it can also be understood

Table 1 Lowest lying excited states of the CO₂ molecule at the equilibrium geometry of the ground state. Labels are reported considering three point groups for CO₂, linear geometry ($D_{\infty h}$ point group) and symmetry of a single plane (C_s point group). The most contributing orbital vertical transitions that yield the excited state are quoted using the C_s labels (energy degeneracies quoted in Fig. 1 are considered). Vertical excitation energies ΔE_X (in eV) (computed with $X = \text{EOM-CCSD}$ and $X = \text{MRCI}$) from the ground state are taken at the optimized equilibrium geometry of CO₂ electronic ground state ($R_{\text{CO}} = 2.2$ bohr). State-to-state transition dipole moments μ (a.u.) and oscillator strengths f (a.u.) at the MC/CASSCF level are also reported. Notation $(-x)$ indicates 10^{-x} . Vertical energies ΔE_X have been corrected with the zero point energies in order to compare with the energies ΔE_{exp} obtained from the absorption spectrum²⁷

| $D_{\infty h}$ | C_s | Excitation | $\Delta E_{\text{EOM-CCSD}}$ (eV) | ΔE_{MRCI} (eV) | ΔE_{exp} (eV) | μ (a.u.) | f (a.u.) |
|-----------------|---------------|---|-----------------------------------|-------------------------------|------------------------------|--------------|------------|
| $X^1\Sigma_g^+$ | | X^1A' Ground state | 0.0 | 0.0 | | 0.000 | 0.000 |
| $1^1\Pi_g$ | $1^1A''$ | $2a'' \rightarrow 10a'$ or $9a' \rightarrow 10a'$ | 8.84 | 8.87 | | 0.000 | 0.000 |
| $1^1\Sigma_u^-$ | $2^1A''$ | $2a'' \rightarrow 16a'$ or $9a' \rightarrow 6a''$ | 8.95 | 9.06 | | 0.000 | 0.000 |
| | $1^1\Delta_u$ | $3^1A'$ $9a' \rightarrow 6a''$ or $2a'' \rightarrow 6a''$ | 9.08 | 9.33 | | 0.000 | 0.000 |
| $1^1\Sigma_u^+$ | | $4^1A'$ $9a' \rightarrow 11a'$ | 11.02 | 10.93 | 11.04 | 0.642 | 0.175 |
| | $2^1\Delta_u$ | $4^1A''$ $9a' \rightarrow 3a''$ or $2a'' \rightarrow 3a''$ | 11.10 | 11.00 | | 0.000 | 0.000 |
| $2^1\Sigma_u^-$ | | $5^1A'$ $2a'' \rightarrow 11a'$ | 11.15 | 11.02 | | 0.000 | 0.000 |
| | $1^1\Pi_u$ | $6^1A''$ $2a'' \rightarrow 12a'$ or $9a' \rightarrow 12a'$ | 11.38 | 11.13 | 11.39 | 0.126 | 0.035 |
| | $2^1\Pi_g$ | $7^1A''$ $2a'' \rightarrow 15a'$ or $9a' \rightarrow 15a'$ | 11.87 | 11.84 | | 1.72(-6) | 0.000 |
| | $3^1\Pi_g$ | $8^1A''$ $9a' \rightarrow 5a''$ or $2a'' \rightarrow 5a''$ | 12.17 | | | 0.000 | 0.000 |
| | $4^1\Pi_g$ | $9^1A''$ $2a'' \rightarrow 14a'$ or $9a' \rightarrow 14a'$ | 12.18 | | | 0.000 | 0.000 |
| | $1^1\Delta_g$ | $10^1A''$ $2a'' \rightarrow 13a'$ or $9a' \rightarrow 13a'$ | 12.25 | | | 0.000 | 0.000 |
| | | $11^1A''$ $2a'' \rightarrow 15a'$ or $9a' \rightarrow 15a'$ | 12.26 | | | 0.000 | 0.000 |
| $1^1\Sigma_g^+$ | | $12^1A''$ $9a' \rightarrow 4a''$ | 12.27 | | | 0.000 | 0.000 |
| $2^1\Sigma_g^+$ | | $12^1A'$ $9a' \rightarrow 13a'$ | 12.30 | | | 0.000 | 0.000 |
| $2^1\Sigma_g^-$ | | $13^1A'$ $9a' \rightarrow 16a'$ or $2a'' \rightarrow 6a''$ | 12.47 | | 12.51 | 1.977 | 0.609 |
| $2^1\Sigma_g^-$ | | $8a' \rightarrow 6a''$ or $1a'' \rightarrow 16a'$ | 12.98 | | | 3.72(-5) | 1.22(-5) |
| | $2^1\Pi_u$ | $14^1A''$ $1a'' \rightarrow 16a'$ or $8a' \rightarrow 16a'$ | 13.23 | | 12.63 | 6.31(-4) | 2.06(-4) |

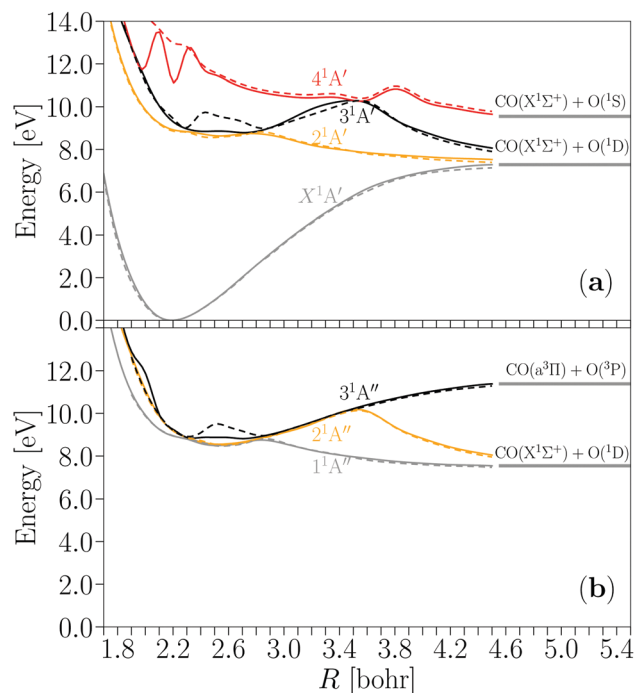


Fig. 2 Potential energy curves for the ground state X^1A' and the three lowest singlet excited states of symmetry A' (a) and A'' (b). The adiabatic energies of two types of calculations using the MCSCF/MRCI level of theory (see the main text) are compared in the figures: full valence active space FVAS (16,12) (dashed lines) and partial valence active space PVAS (12,11) (solid lines) [the latter including a Rydberg orbital $10a'$ in the active space]. Here coordinate R corresponds to one CO distance whereas the other CO is kept fixed to $R = 2.2$ bohr. The OCO angle = 179.99° .

as though the basis that yields Rydberg states is projected out) within the active space in the FVAS calculation avoids the variational collapse to lower (Rydberg) states of the same symmetry $1A'$. Rydberg orbitals (almost atomic in nature) do their best job at small internuclear distances and specifically in the FC region, which is of utmost importance for the study of VUV photoabsorption in CO₂. Therefore, an efficient way to produce a full set of Rydberg states within the FC region now becomes worthy of exploration, in order to find not only their energy location but also their oscillator strengths that determine their role in the photoabsorption along with the valence states.

Given the nature of Rydberg orbitals, mostly relevant at short internuclear distances, their role in the shape of the conical intersection [item (iii)] and the potential barrier [item (iv)] is much less relevant. However, since Rydberg states stabilize at short distances but they correlate to much higher fragmentation channels, their trend is to intercept cross diabatically the valence states that contribute to the lower fragmentation channels. Thus an intricate plethora of Rydberg states are expected to contribute to the VUV absorption and ultimately to the fragmentation.

Now, to increase the active space with a full set of Rydberg orbitals plus the valence orbitals becomes computationally prohibitive within the MCSCF/MRCI method and a different approach must be envisaged to uncover and characterize those Rydberg states intertwined with valence states. We choose the method equation of motion with coupled cluster single and double excitations (EOM-CCSD).²⁸ Despite the lack of orbital optimisation, EOM-CCSD allows for a much large number of excitations, which is an advantage for highly excited Rydberg states. On the other hand, EOM-CCSD uses orbitals obtained

from the ground state, and the energies deteriorate far away from the equilibrium geometry and they do not provide the correct asymptotic dissociation energies. However, our interest is to disclose Rydberg states in the FC region, prior to their crossing with the valence states, since this is the relevant part involved in the VUV photoabsorption.

We compute up to seventeen excited states using EOM-CCSD, considering a vertical transition ΔE from the ground state at the equilibrium geometry. We are aware that many excited states in CO_2 are bent states, but for a prompt photoabsorption with an ultrashort laser pulse relaxation of excited states is not relevant at this stage, as established in the theoretical and experimental work by Lu *et al.*¹ In Table 1 we give the electronic transition energies ΔE , the leading orbital transitions characterizing the excited state (mind the energy degeneracies of orbitals) along with the dipole moment and oscillator strength for the transition from the ground state. We have included the IR of these eighteen states for two point groups ($D_{\infty h}$ and C_s) in order to compare with other previous calculations in the literature.^{5,6,8,11,29} From the list of excited states and their characterization in terms of orbital excitations we arrive at the conclusion that most of the excited states in the VUV region (11–13 eV) are in fact Rydberg molecular states. The lowest excited states $2^1A'$ and $1^1A''$ already have an important Rydberg contribution because of the HOMO–LUMO $\{9a', 2a''\} \rightarrow 10a'$ transition. At variance, the next states $2^1A''$ and $\{3^1A', 3^1A''\}$ involve transitions from the HOMO to valence orbitals $16a'$ and $6a''$. The next eleven states are all Rydberg states. The next valence state is $13^1A'$, that in fact corresponds to the $4^1A'$ state calculated by the MCSCF/MRCI method using FVAS(16,12). Beyond this state we find two additional valence states. At first glance, Table 1 gives an idea of the intricate landscape of excited states in CO_2 , dominated mostly by Rydberg states. However, we also find that not all of them are relevant in photo-absorption due to the corresponding small or even negligible oscillator strength. From the dipole moment values it is clear that in the VUV region of interest (11–13 eV) the upper valence state $13^1A'$ will take the largest absorption. Nevertheless, the direct excitation to Rydberg states $4^1A'$, $6^1A'$, and $6^1A''$ should not be neglected *a priori* in photo dynamical calculations. Notice also that the absorption to the next valence states $13^1A''$ (strictly forbidden in $D_{\infty h}$) and $14^1A'$, $14^1A''$ ($X^1\Sigma_g^+ \rightarrow 2^1\Pi_u$ perpendicular transition) are almost negligible in this energy region. In conclusion we now better understand on a proper *ab initio* footing the leading relevance of the $13^1A'$ valence state in the photodissociation of CO_2 (Lu *et al.*¹ put a label $4^1A'$ to this state since they did not include explicitly the Rydberg states).

Finally, we have extended the EOM-CCSD calculation to a set of CO bond distances $R \in [1.7, 4.6]$, which allows us to compare in Fig. 3 the potential energy curves obtained with EOM-CCSD and with MCSCF/MRCI using PVAS (12,11). Whereas EOM-CCSD energies for excited states clearly tend to incorrect asymptotic dissociation limits, they show an excellent smooth behaviour at shorter distances for both $^1A'$ and $^1A''$ states. In particular, it is worth noting that the spurious oscillations in the energies present in the $4^1A'$ state fully disappear when using

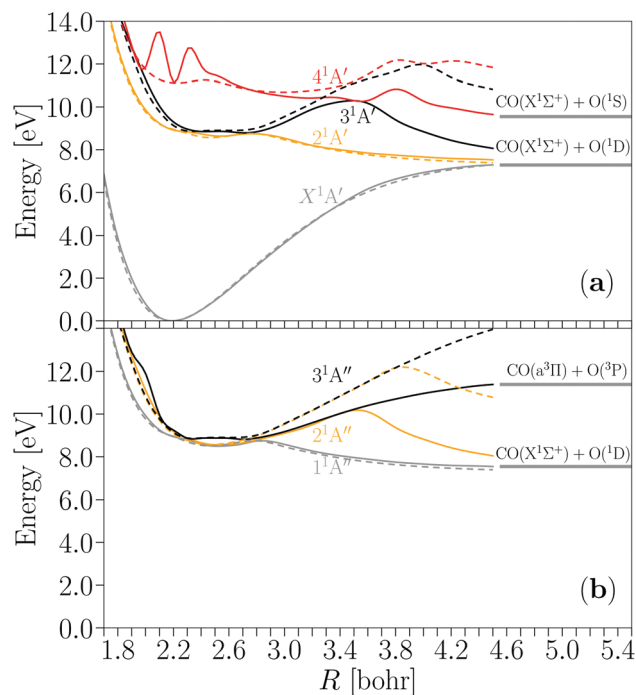


Fig. 3 Same as Fig. 2 where curves are calculated at the MCSCF/MRCI level of theory with a PVAS (12,11) (solid lines) and using EOM-CCSD (dashed lines), including all valence and Rydberg orbitals quoted in Fig. 1.

the EOM-CCSD method (that accounts for the correct Rydberg orbital excitations). Also, those spurious wiggle between the two avoided crossing associated with pairs $\{2^1A'-3^1A'\}$ and $\{1^1A''-2^1A''\}$ disappears in the EOM-CCSD energies.

3 Photofragmentation dynamics in the Rydberg energy region

Computing photodynamics in CO_2 from a full *ab initio* perspective is still a formidable task at present. It involves obtaining accurate potential energy surfaces in terms of the two bond lengths R_1 (O–CO) and R_2 (OC–O) and the bending angle θ (O \hat{C} O). Lu *et al.*¹ computed several cuts of the PES of valence states, keeping R_1 fixed and with the variation of (R_2, θ) . The inspection of these cuts provided information about the small variation of energies with the bond angle and that the relevant features for the dissociation OC–O along R_2 at the equilibrium distance $R_1 = 2.0$ bohr remain similar across different cuts for $2.0 < R_1 < 2.4$ bohr. It makes it plausible to propose a one-dimensional model for these photodissociation channels. From our previous section we have uncovered the presence of molecular Rydberg excited states within the FC region. Obtaining an accurate 3D PES (including Rydberg states) is not affordable using MCSCF/MRCI methods because of the required large active space. If the computations were possible, the participation of so many intruder Rydberg states with the same symmetry produces a large number of conical intersections, that require a diabaticization procedure to allow for a multidimensional wave packet dynamics. Therefore, since the 1D approximation has

been well justified for CO₂ fragmentation into CO + O, we follow along these steps.

For the sake of simplicity we assume that the CO₂ molecule remains linear during the prompt excitation and dissociation (a fact that is supported experimentally)¹ and in addition we consider CO₂ a fixed-in-space molecule, excited by an ultrashort laser with the polarization direction along the molecular axis, so that only $\Sigma_g^+ \rightarrow \Sigma_u^+$ ($A' \rightarrow A'$) photoexcitations occur. Furthermore, radial non-adiabatic couplings lead to mixing of states with the same symmetry. Once excited, effects like non-adiabatic Coriolis couplings or Renner–Teller couplings could mix Σ_g^+ (A') and Π states (A' and A''), but these effects (if any) would require times much longer than the first stages of dissociation under consideration in this work. Also, the experiment in CO₂ by Lu *et al.* (2015) clearly demonstrated that dissociation to form O(¹D) and O(¹S) channels is faster than the rotational periods of VUV excited CO₂ molecules, so that Coriolis-like couplings involving excited states do not add to the fragmentation dynamics in the lower channels. All this justifies our approach within the A' manifold of states only. Along this direction, we have checked that excitation to the $6^1A'$ and $14^1A'$ states (components of the $1^1\Pi_u$ and $2^1\Pi_u$, respectively) is almost negligible in comparison to other $A'(\Sigma_u^+)$ excitations.

3.1 Diabatization procedure

Even in the case of 1D multistate quantum dynamic calculations the presence of both valence and Rydberg states and their ensuing avoided crossings require a sort of strategy to deal with a series of non-adiabatic couplings. In addition, as shown in the previous section, potential energy curves calculated using EOM-CCSD are very satisfactory in the FC region, but their dissociation trends are wrong, whereas potential energy curves computed at the MRCI level provide the correct asymptotic behavior. Here we propose a matching procedure between EOM-CCSD eigensolutions at the inner region ($R < 2.7$ bohr) and MRCI eigensolutions at the outer region ($R > 2.7$ bohr). Thus we have extended the EOM-CCSD calculations for the fourteen lowest states $^1A'$ and $^1A''$ for $1.7 < R < 3.4$ bohr, thus

covering the inner region. EOM-CCSD potential energy curves are included in the Fig. 4.

Dynamic calculations based on adiabatic states could be feasible in 1D provided all non-adiabatic couplings (NAC) $f_{ij}(R)$ are computed accurately and included in the equations. However, these functions $f_{ij}(R)$ are usually peaked functions at the internuclear distance where energies E_i and E_j display an avoided crossing. Ultimately integration along these functions is complicated, which leads us to the choice of a diabatic basis of states. Furthermore, the computation of NAC is possible using the MRCI/CASSCF theory, but the huge number of configurations required to compute the lowest fourteen A' and A'' states, make this approach unfeasible to obtain NACs for the higher Rydberg and valence states. Also, the computation of NACs within the EOM-CCSD method of solution is not implemented in MOLPRO albeit implementations are available based on QChem.³⁰ Here, we choose instead to follow an *ad hoc* diabaticization procedure without explicit NACs.

Firstly, we make a choice of the essential states involved in any photoabsorption process from the ground state, for photon energies below 13 eV. To simplify, we assume polarization along the x , y directions so that allowed transitions are $A' \rightarrow A'$. From the oscillator strengths quoted in Table 1 the relevant bright states within the A' symmetry are 4, 6 and $13^1A'$. We have excluded the $14^1A'$ state for three reasons: first, although the lower Rydberg state $6^1A'$ and the lower valence state $13^1A'$ originate from orbital excitations involving the HOMO $9a' \rightarrow na'$, the $14^1A'$ state involves excitation from the HOMO–1 $8a' \rightarrow na'$, it results in a much smaller dipole strength within the FC region; second, this valence state shows a smaller FC factor and it does not dissociate adiabatically to the lowest fragmentation channel, of our prime interest in this work; third, this $14^1A'$ is a component of the $2^1\Pi_u$ state, that is not photoexcited if light polarization is along the molecular axis. The n^1A' ($n = 7$ –12) Rydberg states are dark states for an excitation from the ground state. However, they may eventually participate in the subsequent internal conversion from the main excitation to the $13^1A'$ state through a series of multilevel

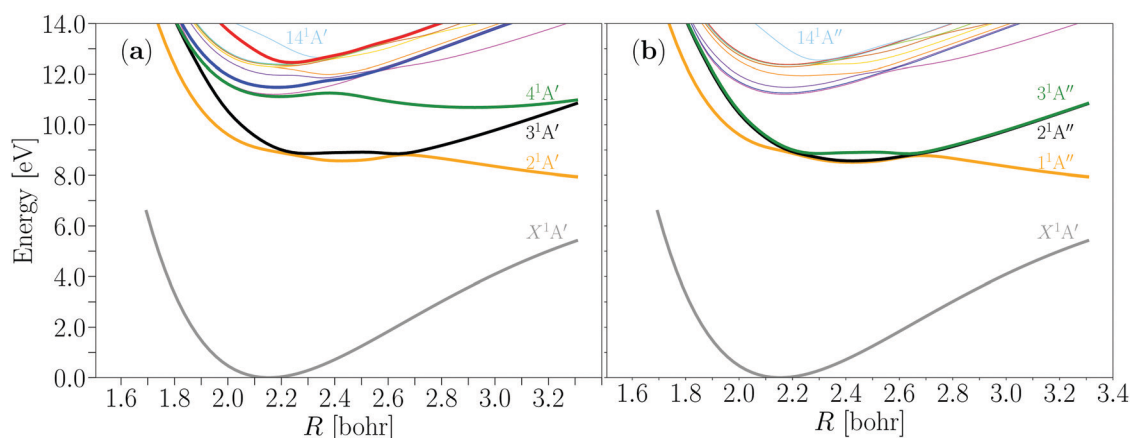


Fig. 4 Adiabatic potential energy curves for (a) the ground state X^1A' and the lowest thirteen excited states $^1A'$ and (b) the ground state X^1A' and the lowest fourteen excited states $^1A''$, as calculated at the EOM-CCSD level of theory.

crossings. To simplify the dynamics we proceed through an effective *pseudo-diabatization* procedure between the $4^1A'$, $6^1A'$ and $13^1A'$ states that approximates the ladder crossings between intermediate n^1A' ($n = 7-12$) dark Rydberg states (see below).

Once the set of essential states is chosen we proceed to the inner-outer matching procedure, which is illustrated in Fig. 5. We find the smoothest connection between the EOM-CCSD and the MRCI/CASSCF energies located at $R \sim 2.8$ bohr. Now, although n^1A' ($n = 7-12$) Rydberg states are excluded from the set of essential states, their presence modifies the valence state $13^1A'$ due to multilevel crossings shown in Fig. 4. In fact, any molecular property (for instance dipoles) computed using the adiabatic $13^1A'$ state in Fig. 5(a) shows abrupt discontinuities along the internuclear distance in the FC region. To cure this situation, we choose to follow a *pseudo-diabatization* procedure by fixing the main electronic excitation. For the sake of clarity, the states $4^1A'$, $6^1A'$ and $13^1A'$ are characterized by the main orbital excitations $9a' \rightarrow 11a'$, $9a' \rightarrow 12a'$ and $9a' \rightarrow 16a'$ at $R = 2.2$ bohr (equilibrium geometry). At larger internuclear distances $R = 2.3, 2.4, \dots$ bohr we connect the energies of states preserving the same electronic excitation character, irrespective of their label state n^1A' ($n = 6-14$). After this procedure, the $4^1A'$ state barely changes, the $6^1A'$ state is slightly modified but the

valence state $13^1A'$ is instead notoriously changed [see Fig. 5(a) and (b)], and as a result it brings the multilevel Rydberg crossings to an effective single valence state. Now, this state presents a clear avoided crossing with the lower Rydberg $6^1A'$ state. Note that the $13^1A'$ state remains in the adiabatic state within the set of essential states, as shown in Fig. 5(b).

To proceed now with a diabaticization procedure within the set of six essential states, we consider successive unitary transformations between any two i, j coupled states. Because of the NAC at the avoided crossing region, adiabatic states Ψ_i^{ad} and Ψ_j^{ad} are mixed in the form $\Psi_i^{\text{ad}}(R + dR) \simeq \Psi_i^{\text{ad}}(R) + \Psi_j^{\text{ad}}(R)d\theta$ and $\Psi_j^{\text{ad}}(R + dR) \simeq \Psi_j^{\text{ad}}(R) - \Psi_i^{\text{ad}}(R)d\theta$ from which one obtains the radial matrix element $\left\langle \Psi_i^{\text{ad}} \left| \frac{\partial}{\partial R} \right| \Psi_j^{\text{ad}} \right\rangle = -\frac{d\theta(R)}{dR} = f_{ij}(R)$, which indicates that the variation $d\theta/dR$ corresponds to the NAC function $f_{ij}(R)$. In general, following the work by Smith³¹ the change from adiabatic to diabatic bases involves an unitary transformation $\Psi_i^{\text{dia}}(R) = \sum_k U_{ik}(R) \Psi_k^{\text{dia}}(R)$, where $U(R)$ can be set as an 2×2 rotation matrix whose rotation angle corresponds to the angle integrated from the radial NAC, *i.e.*, $\theta(R) = -\int_0^R R' f_{ij}(R') dR'$. This transformation is optimized to yield zero NAC in the new diabatic basis at the expense of electrostatic couplings, which amounts to modify the potential energies. To generalize the 2×2 to a $n \times n$ unitary transformation for a set of n adiabatic states, the potential energies curves are transformed using successive rotations along the internuclear distance R

$$\mathbf{V}^{\text{dia}}(R) = \left(\prod_{k=1}^{n(n-1)/2} \mathbf{U}_{ik,jk}^T[\theta_k(R)] \right) \mathbf{V}^{\text{ad}}(R) \left(\prod_{k=1}^{n(n-1)/2} \mathbf{U}_{ik,jk}[\theta_k(R)] \right) \quad (5)$$

where \mathbf{V}^{dia} and \mathbf{V}^{ad} correspond to the diabatic and adiabatic potential energy matrices, respectively, and a transformation angle θ_k for any two states i, j (coupled or not). For our set of essential states, they have the diagonal form $\mathbf{V}(R) = \text{diag}(V_{1A'}(R), V_{2A'}(R), V_{3A'}(R), V_{4A'}(R), V_{6A'}(R), V_{13A'}(R))$ and the rotation matrix k for a given pair i, j reads

$$\mathbf{U}_{ik,jk}[\theta_k(R)] = \begin{pmatrix} \cdots & i_k & \cdots & j_k & \cdots \\ \vdots & \vdots & \cdots & \vdots & \cdots \\ i_k & \cdots & \cos[\theta_k(R)] & \cdots & \sin[\theta_k(R)] & \cdots \\ \vdots & \cdots & \vdots & \ddots & \vdots & \cdots \\ j_k & \cdots & -\sin[\theta_k(R)] & \cdots & \cos[\theta_k(R)] & \cdots \\ \vdots & \cdots & \vdots & \cdots & \vdots & \ddots \end{pmatrix} \quad (6)$$

In practice, in the present case, index k only runs for those pairs with non-negligible NAC [mostly around avoided crossings in Fig. 5(b)].

The exchange of character between adiabatic states at avoided crossings can also be uncovered by the behavior of any molecular

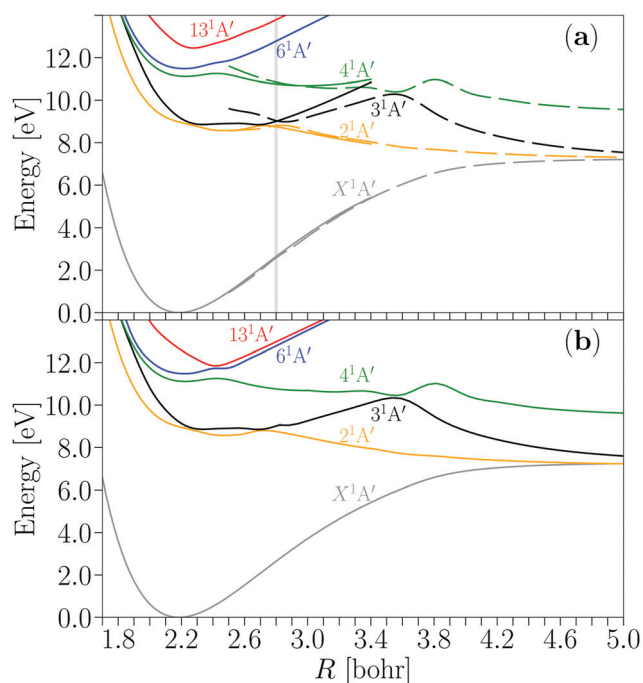


Fig. 5 (a) Potential energy curves for $1^1A'$, $2^1A'$, $3^1A'$, $4^1A'$, $6^1A'$ and $13^1A'$ states calculated with EOM-CCSD for distances $1.7 < R < 3.4$ bohr (solid lines) and calculated with MRCI/CASSCF for distances $2.5 < R < 5.3$ bohr (dashed lines). Vertical gray line located at $R \sim 2.8$ bohr indicates the matching point for a smooth connection between the inner region calculated with EOM-CCSD ($R < 2.8$ bohr) and the outer region calculated with MRCI/CASSCF ($R > 2.8$ bohr). (b) Same as (a) where a softened energy matching is made at $R = 2.8$ bohr and an effective *pseudo-diabatization* that involves the $4^1A'$, $6^1A'$ and $13^1A'$ states is made at the edge of the FC region (see text).

property, like dipole moments. For instance, permanent dipole moments $\hat{\mu}_{ii}^z(R)$ in the adiabatic representation of the dipole operator $\hat{\mu}^{\text{ad}}$ are displayed in Fig. 6(a) for the $2^1\text{A}'$, $3^1\text{A}'$ and $4^1\text{A}'$ states. The exchange in the dipoles between the states $2^1\text{A}'$ and $3^1\text{A}'$ at $R \sim 2.3$ bohr and $R \sim 2.7$ bohr comes from the corresponding NAC at the avoided crossings located at those internuclear distances. Similarly it happens for the dipoles between $3^1\text{A}'$ and $4^1\text{A}'$ at $R \sim 3.6$ bohr. Then dipoles could also be used to find the transformation angle $\theta_k(R)$. Adiabatic dipole matrices $\hat{\mu}^{\text{ad}}$ with elements $\hat{\mu}_{ij}^{\text{ad},z}(R) = \langle \Psi_i^{\text{ad}} | \hat{\mu}^z | \Psi_j^{\text{ad}} \rangle$ in the adiabatic representation can be brought to its diabatic form $\hat{\mu}^{\text{d}}$ by diagonalizing the dipole matrix. Angle $\theta^{\text{d}}(R)$ for the rotation that brings the 2×2 matrix $\hat{\mu}^{\text{ad}}$ to its diagonal form is given by

$$\theta(R) = \begin{cases} \frac{1}{2} \tan^{-1} \left(\frac{2\mu_{ij}(R)}{\mu_{ii}(R) - \mu_{jj}(R)} \right) & R \leq R_C \\ \frac{1}{2} \tan^{-1} \left(\frac{2\mu_{ij}(R)}{\mu_{ii}(R) - \mu_{jj}(R)} \right) + \frac{\pi}{2} & R > R_C \end{cases} \quad (7)$$

where R_C corresponds to the internuclear distance where the potential energy curves show the peak of the NAC at the avoided crossing. The term $\pi/2$ in eqn (7) accounts for the exchange of character at the anticrossing point R_C . To simplify this approach,

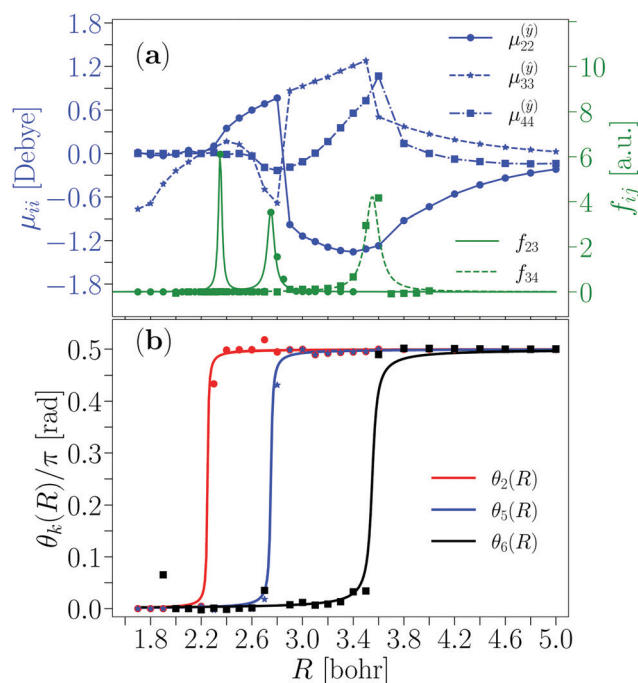


Fig. 6 (a) Adiabatic diagonal (permanent) dipole moments $\hat{\mu}_{ii}^z$ for the electronic states $2^1\text{A}'$, $3^1\text{A}'$ and $4^1\text{A}'$ along the molecular z axis. Blue symbols represent *ab initio* values obtained at each calculated R point. Lines in blue correspond to a smooth interpolation of *ab initio* data. Non adiabatic coupling $f_{ij}(R)$ between the states $2^1\text{A}'$ and $3^1\text{A}'$ and between $3^1\text{A}'$ and $4^1\text{A}'$ states are also included. Green symbols correspond to *ab initio* values whereas solid lines in green are smooth fittings. (b) Rotation angles $\theta_k(R)$ for adiabatic to diabatic transformations. Dots correspond to values of $\theta_k(R)$ obtained by diagonalizing the adiabatic dipole matrix and solid lines correspond to an interpolation using our two-parameter arctan model function (see text).

Table 2 Parameters used in the arctan model in eqn (8) for the rotation angle $\theta_k(R)$ employed in the diabaticization procedure for a series of k couplings between states i_k and j_k

| k | R_{C_k} [bohr] | i_k | j_k | β_k |
|-----|------------------|----------------|-----------------|-----------|
| 1 | 1.90 | $3^1\text{A}'$ | $4^1\text{A}'$ | 44.0 |
| 2 | 2.25 | $2^1\text{A}'$ | $3^1\text{A}'$ | 145.0 |
| 3 | 2.35 | $6^1\text{A}'$ | $13^1\text{A}'$ | 50.0 |
| 4 | 2.45 | $4^1\text{A}'$ | $6^1\text{A}'$ | 40.0 |
| 5 | 2.75 | $2^1\text{A}'$ | $3^1\text{A}'$ | 90.5 |
| 6 | 3.55 | $3^1\text{A}'$ | $4^1\text{A}'$ | 35.5 |

since the NAC $f_{ij}(R)$ behaves approximately as Lorentzian functions it is straightforward to introduce a simple arctan model function with a single fitting parameter for any two coupled states, in the form

$$\theta_k(R) = \frac{1}{2} \tan^{-1} [\beta_k(R - R_{C_k})] + \frac{\pi}{4}, \quad (8)$$

where R_{C_k} is the position of each anticrossing point between two electronic states and β_k is a fitting parameter. Parameters for this model within our set of essential states are included in Table 2. Rotation angles obtained from dipoles in eqn (7) and from the arctan model in eqn (8) are compared in Fig. 6(b). Finally, using this direction we obtain the set of essential states in their diabatic representation, and the new potential energy curves are shown in Fig. 7, where avoided crossings are replaced by real crossings and the states display very smooth connections.

3.2 Photodynamics of CO_2 using ultrashort laser pulses

Instead of using perturbative continuous wave lasers, we subject CO_2 to ultrafast photodynamics driven by an ultrashort intense laser pulse. From the theoretical point of view it means that one is subject to solve the time-dependent Schrödinger equation to deal with the ensuing nonlinear effects. Intense short pulses in the fs and as time window are produced at present routinely in many laboratories, for instance, in pump-delay-probe protocols.^{32,33} Their advantage is two-fold: they allow to unveil, follow and even control the fast inner workings of molecular motions (electronic and nuclear) and ultrashort pulses allow for a wider excitation energy window, so that a manifold of excited states could be simultaneously excited and several reaction paths may interfere in a full dynamics. In addition, the use of ultrashort pump laser pulses produces a prompt excitation and the subsequent non-adiabatic molecular dynamics is field-free.

We make use of a set of six essential states of symmetry $1^1\text{A}'_d$ from the previous electronic structure study, and then 1D nuclear dynamics will run over the diabatic basis built in Fig. 7. To solve the nuclear photodynamics we use a wavepacket propagation method based on a DVR basis, as implemented in the freely available MCTDH software package.¹³ For instance, some of us recently used this code to solve *ab initio* polariton photodynamics of diatomic molecules.^{34–37} In our grid-based calculations the degree of freedom R corresponding to the bond distance CO is represented with a sin-DVR primitive basis using 1061 grid points between $R = 1.7$ bohr and $R = 7.0$ bohr. We perform multistate calculations by including the set of six

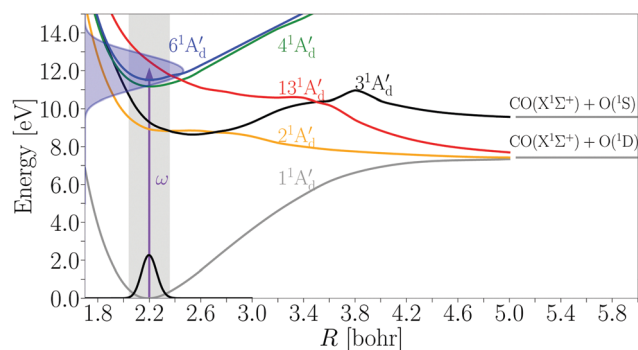


Fig. 7 Molecular diabatic electronic states of the symmetry $1A'$. States $1^1A'$, $3^1A'$ and $13^1A'$ correspond to valence states and $2^1A'$, $4^1A'$ and $6^1A'$ correspond to Rydberg states. The band in grey represents the Franck–Condon region. The vertical blue arrow indicates the laser excitation with a central photon frequency $\omega = 12$ eV and the Fourier transform of the laser pulse with a duration $T = 3$ fs indicates the energy window of the excitation along the y-axis.

essential states in their diabatic form. Then the total time dependent wavepacket (WP) is represented with the ansatz

$$\Psi(R, t) = \sum_{\alpha=1}^{N_{\alpha}} A^{\alpha}(t) \phi^{\alpha}(R, t) \quad (9)$$

where $N_{\alpha} = 6$ is the number of electronic states and $\phi^{\alpha}(R, t)$ corresponds to the single particle function (due to the reduced dimensionality the partial nuclear WP for each electronic state is represented by a single particle function). The reduced mass used for the CO bond was set at $\mu = 10.18$ amu. To simulate the dissociation probability we assume that the portion of the WP $A^{\alpha}(t) \phi^{\alpha}(R, t)$ crossing a given outer internuclear distance C–O goes to dissociation in an irreversible way. This is ultimately calculated by considering the flux that meets an absorbing boundary potential located at $R = 5$ bohr (a distance that the WP reaches within ~ 20 – 25 fs). The MCTDH package allows introducing external interactions like laser pulses that we simulate here with an electric field $E(t) = E_0 f(t) \sin(\omega t + \phi) \hat{e}_z$ (E_0 is the field amplitude, ω is the central frequency, \hat{e}_z is the polarization unit vector and ϕ is the phase) with a chosen shape function $f(t) = \sin^2\left[\frac{\pi t}{T}\right]$ with $t \in [0, T]$. We use a central photon frequency $\omega = 12$ eV and a short pulse duration of $T = 3$ fs that produces an energy bandwidth within the FC region of ~ 2 eV (see Fig. 7). Using a light polarization along the molecular axis, two states $4^1A'_d$ (Rydberg) and $13^1A'_d$ (valence) are simultaneously populated by the short pulse (the $6^1A'_d$ Rydberg state contributing to $1^1\Pi_u$ is removed only from the excitation process).

Due to NAC at multilevel crossings, the molecular Rydberg states n^1A' , $1A''$ ($n = 2, 4, 6$ – 12) in CO_2 behave as metastable states, *i.e.*, they can be populated by any unpolarized radiation but eventually they will not keep much of this population, which is eventually transferred to the leading dissociating valence states. Thus Rydberg states are expected to decay with a given lifetime into the robust valence state. Due to the highly

nonlinear nature of multilevel non-adiabatic dynamics, this decay is non-exponential. Also, these Rydberg states are not only populated directly by the laser field, they can also be populated from the valence state $13^1A'_d$ due the same NAC. To illustrate the role of the Rydberg states in the dynamics we have performed three types of calculations: type I, in which we assume that the radiation has fully excited the molecule to the valence state $13^1A'_d$, *i.e.*, the initial WP located at this state is a carbon copy of the vibrational ground state in the X^1A' state; type II, we perform a calculation with an explicit excitation by the ultrashort intense laser pulse; and type III, using the same laser pulse but with all Rydberg states removed from the calculation. In Fig. 8(a) we have included the time evolution of populations and fragmentation yields from the three calculations.

• **Type I.** We note that from the very start $t = 0$ the population of the $13^1A'_d$ valence state promptly reduces by around 20%, mainly in favor of the Rydberg states $6^1A'_d$ and $4^1A'_d$ (the transfer to the former is almost immediate and to the latter is delayed by ~ 4 – 5 fs) with a population ratio between these Rydberg states that depends upon the strength of their respective electrostatic diabatic couplings. Once the WP starts in the $13^1A'_d$ state, it moves toward dissociation since it is a repulsive state. The WP rapidly reaches the crossing $R_C = 2.35$ bohr with the $6^1A'_d$ state, and then crosses the $4^1A'_d$ at $R_C = 2.45$ bohr. These couplings explain the sequential rise of populations of these two Rydberg states. Then the population remains steady until $t = 15$ fs when the WP reaches the crossing at $R_C = 3.55$ bohr between $13^1A'_d$ and $3^1A'_d$, that makes a very small transfer to the $3^1A'_d$ state. From $t = 15$ to $t = 20$ – 25 fs the dissociating WP arrives the complex absorbing potential ($R_{\text{CAP}} = 5$ bohr), where almost the total population of the $13^1A'$ state contributes to the dissociation yield into the $\text{CO}(^1\Sigma^+) + \text{O}(^1\text{D})$ channel [see Fig. 8(b)]. However, after $t = 30$ fs we can appreciate an enhancement in the population of the $13^1A'_d$ state [Fig. 8(a)], while the dissociation yield coming from the same state remains constant within the time interval $t = 25$ – 50 fs. We have checked out that this population enhancement of the $13^1A'$ state comes from the leaking of the remnant partial WP oscillating to and fro within the $4^1A'_d$ and $6^1A'_d$ Rydberg potential energy curves. This newly generated partial WP on the $13^1A'$ state promptly leads to dissociation and it reaches the CAP located at 5.0 bohr when $t \sim 50$ fs. Consequently the dissociation yield through $13^1A'_d$ increases at $t = 50$ fs, as shown in Fig. 8(b). Every 25 fs there will be a similar increase in the dissociation yield, that occurs due to the same leaking process from the intermediate Rydberg states, until they are fully depleted.

• **Type II:** the molecule is excited by a 3 fs laser pulse (we choose the shortest duration T satisfying the π -area theorem to achieve a high transfer to the $13^1A'_d$ state from the ground state). Thus Fig. 8(a) shows clear Rabi oscillations for this valence state with the largest dipole. At the end of the pulse this state reaches

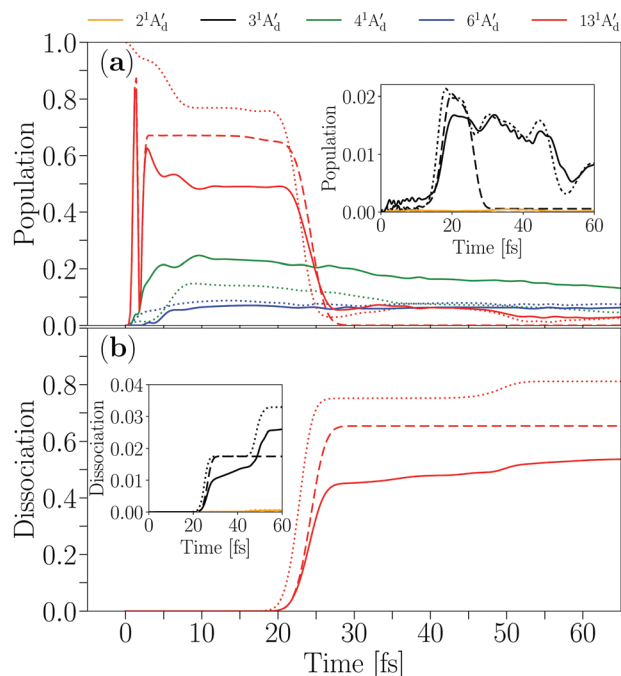


Fig. 8 Time dependent population of essential excited n^1A' states ($n = 2, 3, 4, 6$ and 13) (a) and photodissociation probability (b) in fragments $\text{CO}(^1\Sigma) + \text{O}(^1\text{D})$, via the $13^1A_d'$ state and $\text{CO}(^1\Sigma) + \text{O}(^1\text{S})$, via the $3^1A_d'$ state for three types of calculations: type I: dynamics that starts from the excited valence state $13^1A'$ being fully populated without the laser pulse (dotted lines); type II: photodynamics started from the ground state by an ultrashort laser pulse, with duration $T = 3$ fs, central frequency $\omega = 12$ eV and intensity $3.5 \times 10^{14} \text{ W cm}^{-2}$ (solid lines). In both cases, valence and Rydberg states $4^1A'$ and $6^1A'$ are included explicitly, and type III: data plotted with dashed lines correspond to the type II induced by a laser pulse but eliminating the Rydberg states from the dynamic calculation. The population of $3^1A'$ state in (a) and the dissociation yield in (b) via the $3^1A_d'$ state are displayed in the insets.

60–70% of the total population. At variance with the previous calculation, the Rydberg state $4^1A_d'$ is also populated by the pulse [see populations within the temporal window $t = 0$ –5 fs in Fig. 8(a)]. Just after the pulse the $13^1A_d'$ state transfers population to the $6^1A_d'$ state and from 5 to 10 fs, the $13^1A_d'$ and $4^1A_d'$ states exchange their populations. In fact, the time evolution of the two Rydberg states $4^1A_d'$ and $6^1A_d'$ parallels those of the type I calculation, although here in type II the $4^1A_d'$ population is enhanced because of its larger oscillator strength (see Table 1). Consistently, the dissociation yield coming from the $13^1A'$ state above $t = 25$ fs is smaller than that in type I by a quantity which is not excited by the laser pulse and remains in the ground state. A new feature is that this dissociation yield increases slowly but steadily because the continuous leaking from the remnant WP stalled in the $4^1A_d'$ Rydberg state, now with a larger population than in type I calculation. This type II calculation also shows a similar feature in the dissociation yield at $t = 50$ fs, as expected, with slight differences related to the important role played by the $4^1A_d'$ state when a radiation is present.

• Type III: the removal of the Rydberg states from the calculation makes the mechanism quite straightforward. Once

the laser pulse populates the $13^1A_d'$ state, only ineffective crossing remains with the $3^1A_d'$ state so that both the higher population [Fig. 8(a)] and higher dissociation yield [Fig. 8(b)] (both from the $13^1A_d'$ state) are structureless and steadily constant. Since the metastable Rydberg states eventually will transfer their population to the $13^1A_d'$ valence state the dissociation yield obtained in the type II calculation will reach the value in type III calculation from below in less than 100 fs.

Now we analyze the much smaller yield corresponding to the diabatic state $3^1A_d'$, that connects to the upper channel of $\text{CO}(^1\Sigma^+) + \text{O}(^1\text{S})$ photoproducts. This state is not populated directly from the ground state by the radiation due to the vanishing oscillator strength and, consequently, its population rises because of several non-adiabatic transfers (see Fig. 5): the path (i) $4^1A' \rightarrow 3^1A'$ at $R = 1.90$ bohr; the path (ii) $13^1A' \rightarrow 6^1A' \rightarrow 4^1A'$ at $R = 3.25$ and $R = 2.46$ bohr then follow path (i) and path (iii) $4^1A' \rightarrow 3^1A'$ at $R = 3.55$ bohr. The type III calculation (laser pulse but no Rydberg state included) represents the simplest dynamic case, and our results in the inset in Fig. 8(a) indicate that the $3^1A_d'$ state is populated at $t \sim 15$ fs, when the nuclear wave packet reaches the crossing $13^1A_d' - 3^1A_d'$ at $R = 3.55$ bohr and subsequently this maximum population (that amounts 0.02) transfers to dissociation from $t = 20$ fs, just when the transferred WP moving in the $3^1A_d'$ reaches the CAP located at $R = 5$ bohr. The profiles of the population and dissociation curves are structureless. From the type I calculation (initial conditions on the $13^1A_d'$ state including the Rydberg state) we learn that whereas the dynamics remains quite similar to that of type I in the time interval $t = 0$ –20 fs, the results clearly differ from $t \sim 25$ fs. In type II the $3^1A'$ population does not drop to zero. Since the dissociation yields of type I and type II calculations are the same in the time interval $t = 0$ –40 fs [see the inset in Fig. 8(b)] this means that the transferred WP evolving in the $3^1A_d'$ state does not substantially recedes due to the potential barrier at $R = 3.8$ bohr and most of it moves straightforward to dissociate into the $\text{CO} + \text{O}(^1\text{S})$ channel, so that the increasing population of the $3^1A_d'$ state at $t \sim 30$ fs must come mainly from the population of the Rydberg states $4^1A_d'$ and $6^1A_d'$. The different paths that feed the $3^1A'$ state are prone to interfere and these interferences cause that population to vary. Again, when the new dissociating WP on the $13^1A_d'$ reaches the crossing $R = 3.53$ bohr at $t \sim 43$ fs, there is a small transfer of population to the $3^1A_d'$ state and subsequently the population drops from 0.15 since the transferred WP reaches the CAP, and at that point the dissociation yield increases with a similar step. The type II calculations (laser pulse plus Rydberg states) display a similar behavior, with differences because of the different initial populations distributed by the laser interaction, the much wider the generated WP due to the large energy bandwidth impressed by the ultrashort pulse of 3 fs. This widespread of the WP may provoke

a continuous leak across the CAP due to both fast and slow components, whereas the WP created in type I calculation (without laser) remains more compact. From these calculations we show that the dominant dissociation channel at this excitation energies corresponds to the production of $O(^1D)$ and the yield for the $O(^1S)$ production is much smaller by more than one order of magnitude.

4 Conclusions

The purpose of this work is twofold. First to provide a better understanding of the electronic structure of highly excited states of CO_2 , specially when the Rydberg-valence nature of these states is strongly mixed. Previous calculations reported by Lu *et al.*¹ did not explicitly reveal the role of Rydberg states both in the potential energy curves and the dynamics. Some spurious structures in the energies were caused by the lack of diffuse Rydberg molecular orbitals in the active space. Here we chose the ANO-L basis set supplemented with diffuse (s, p, d) functions to better describe the lowest Rydberg MOs, within a CASSCF/MRCI approach. Due to the presence of many energy roots of Rydberg character, the CASSCF/MRCI requires a huge active space that makes this method prohibitive. We use instead the EOM-CCSD method which allows for a large amount of single excitations to Rydberg orbitals and yields more than reasonable energies in the Franck–Condon region, both for valence and Rydberg states. We report electronic energies for the lowest fourteen A' and A'' states of quasi-linear CO_2 at the equilibrium distance, most of them with a Rydberg nature.

More importantly, we propose a method of solution to compute the time-dependent photodynamics of the dissociation of the CO_2 molecule into $CO + O$ fragments when exposed to photon energies above 12 eV, thus reaching highly excited molecular Rydberg states along with excited valence states. Our strategy consists of separating two different halfspaces: inner space for short distances $R_{CO} < 3.4$ bohr that contains the Franck–Condon region, calculated using the EOM-CCSD method and the outer region with longer distances $R_{CO} > 3.4$ bohr for fragmentation that is computed using the CASSCF/MRCI method since it yields the correct asymptotic fragmentation energies.

From the plethora of Rydberg states we find that many of them behave as dark states due to their negligible oscillator strengths. We propose an effective dynamic model of six active states along with a corresponding diabaticization procedure. Wave packet calculations using ultrashort laser pulses show clear short-time mechanisms involving Rydberg states both due to direct population by the field and due to non-adiabatic transfer from the most populated valence state. Whereas CO_2 shows a prompt dissociation through the $13^1A'_d$ valence state, Rydberg states act as small population reservoirs with lifetimes beyond 100–150 fs, a time-window quite amenable for pump-probe protocols with delays of few fs. After the main straight fragment signal, bursts of delayed dissociation might be detected every ~ 50 fs from the Rydberg states. These ultrafast features within the photodynamic process of CO_2 become of

interest at present with the advent of sub-fs lasers. For instance, the experimental study of ultrafast mechanisms that involve super-excited states of CO_2 is being carried out by Nisoli and coworkers³⁸ by using time-resolved photoelectron spectroscopy and VUV fs pulses. In the photoelectron yields, they report ultrafast oscillations coming from the vibrational structure of a super-excited Rydberg state (above the ionization threshold CO_2^+) which shows a period as fast as 24 fs.

At this point, with this restricted 1D model, we do not obtain state to state excitation yields with vibrational resolution for the $CO(X^1\Sigma^+)(v)$ fragment, as studied in several recent experiments.^{1–3} However, we can predict the branching ratio between the two main dissociation pathways, producing $O(^1D)$ or $O(^1S)$, could be a factor as large as a factor of ~ 30 . To get track of the ultrafast molecular dynamics is very challenging due to the different relaxation pathways after prompt excitation. We hope our proposal will be useful for future studies in photodynamics and fragmentation of simple molecules involving highly excited molecular Rydberg states, since their role could be mapped using experimental pump-probe laser techniques with a few fs resolution.

Conflicts of interest

There are no conflicts to declare.

Acknowledgements

J. L. S.-V. thanks financial support from Vicerrectoría de Investigación at Universidad de Antioquia, Colombia, through Estrategia de Sostenibilidad and CODI Convocatoria Programática Project No. 2017-16348; J. L. S.-V. also gratefully appreciates the stay as visiting professor in the Facultad de Ciencias Químicas at Universidad Complutense de Madrid where part of this work was elaborated. J. F. T. is supported by Agencia Nacional de Investigación y Desarrollo (ANID), Chile, through the Postdoctoral Fellowship Grant No. 3200565. Computer support by V. Vallet and F. Réal (Université de Lille) is gratefully acknowledged. J. T. and D. P. thank D. Duflot and J.-P. Flament (Université de Lille) for fruitful discussions.

References

- 1 Z. Lu, Y. C. Chang, Y. Benitez, Z. Luo, A. B. Houria, T. Ayari, M. M. Al Mogren, M. Hochlaf, W. M. Jackson and C. Y. Ng, *Phys. Chem. Chem. Phys.*, 2015, **17**, 11752–11762.
- 2 J. Zhou, Z. Luo, J. Yang, Y. Chang, Z. Zhang, Y. Yu, Q. Li, G. Cheng, Z. Chen, Z. He, L. Che, S. Yu, G. Wu, K. Yuan and X. Yang, *Phys. Chem. Chem. Phys.*, 2020, **22**, 6260–6265.
- 3 S. Zhang, Y. Wu, Z. Zhang, Z. Luo, Y. Zhao, Z. Li, Y. Chang, J. Yang, G. Wu, W. Zhang, S. Yu, K. Yuan and X. Yang, *J. Chem. Phys.*, 2022, **156**, 054302.
- 4 E. Sakkoula, G. Sharma, X. Wang, S. W. North, D. H. Parker and W. Wei, *Phys. Chem. Chem. Phys.*, 2022, **24**, 2592–2600.
- 5 S. Y. Grebenshchikov, *J. Chem. Phys.*, 2013, **138**, 224106.
- 6 S. Y. Grebenshchikov, *J. Chem. Phys.*, 2013, **138**, 224107.

- 7 S. Y. Grebenshchikov, *J. CO₂ Utilization*, 2016, **15**, 32–40.
- 8 S. Adachi, M. Sato, T. Suzuki and S. Y. Grebenshchikov, *Phys. Rev. A*, 2017, **95**, 033422.
- 9 Y. Song, H. Gao, Y. C. Chang, Z. Lu, C. Y. Ng and W. M. Jackson, *Phys. Chem. Chem. Phys.*, 2014, **16**, 563–569.
- 10 Z. Lu, Y. C. Chang, Q.-Z. Yin, C. Y. Ng and W. M. Jackson, *Science*, 2014, **346**, 61–64.
- 11 R. J. Buenker, M. Honigmann, H.-P. Liebermann and M. Kimura, *J. Chem. Phys.*, 2000, **113**, 1046.
- 12 H. Reisler and A. I. Krylov, *Int. Rev. Phys. Chem.*, 2009, **28**, 267–308.
- 13 G. Worth, M. Beck, A. Jäckle and H. Meyer, The MCTDH Package, version 8.4, 2007, <http://mctdh.uni-hd.de>.
- 14 H.-J. Werner *et al.* MOLPRO, version 2015.1, A package of ab initio programs, 2015, <http://www.molpro.net>.
- 15 G. Herzberg, *Molecular Spectra and Molecular Structure. III. Electronic Spectra and Electronic Structure of Polyatomic Molecules*, Van Nostrand, Princeton, New Jersey, 2006.
- 16 A. Spielfiedel, N. Feautrier, C. Cossart-Magos, G. Chambaud, P. Rosmus, H. Werner and P. Botschwina, *J. Chem. Phys.*, 1992, **97**, 8382–8388.
- 17 R. A. Kendall, T. H. Dunning Jr. and R. J. Harrison, *J. Chem. Phys.*, 1992, **96**, 6796–6806.
- 18 D. E. Woon and T. H. Dunning Jr., *J. Chem. Phys.*, 1995, **103**, 4572–4585.
- 19 P.-O. Widmark, P.-Å. Malmqvist and B. O. Roos, *Theor. Chim. Acta*, 1990, **77**, 291–306.
- 20 T. H. Dunning, *J. Chem. Phys.*, 1989, **90**, 1007–1023.
- 21 D. E. Woon and T. H. Dunning Jr., *J. Chem. Phys.*, 1993, **98**, 1358–1371.
- 22 P. J. Knowles and H.-J. Werner, *Chem. Phys. Lett.*, 1985, **115**, 259–267.
- 23 H. J. Werner and P. J. Knowles, *J. Chem. Phys.*, 1985, **82**, 5053–5063.
- 24 H. J. Werner and P. J. Knowles, *J. Chem. Phys.*, 1988, **89**, 5803–5814.
- 25 P. J. Knowles and H.-J. Werner, *Chem. Phys. Lett.*, 1988, **145**, 514–522.
- 26 T. H. Dunning and P. J. Hay, *Methods of Electronic Structure Theory*, Springer, US, 1977, vol. 3.
- 27 C. Cossart-Magos, M. Jungen and F. Launay, *Mol. Phys.*, 1987, **61**, 1077–1117.
- 28 J. F. Stanton and R. J. Bartlett, *J. Chem. Phys.*, 1993, **98**, 7029–7039.
- 29 P. J. Knowles, P. Rosmus and H. J. Werner, *Chem. Phys. Lett.*, 1988, **146**, 230–235.
- 30 S. Faraji, S. Matsika and A. I. Krylov, *J. Chem. Phys.*, 2018, **148**, 044103.
- 31 F. T. Smith, *Phys. Rev.*, 1969, **179**, 111–123.
- 32 P. Corkum and F. Krausz, *Nat. Phys.*, 2007, **3**, 381.
- 33 A. Palacios, J. L. Sanz-Vicario and F. Martín, *J. Phys. B: At., Mol. Opt. Phys.*, 2015, **48**, 242001.
- 34 J. F. Triana, D. Peláez and J. L. Sanz-Vicario, *J. Phys. Chem. A*, 2018, **122**, 2266–2278.
- 35 J. F. Triana and J. L. Sanz-Vicario, *Phys. Rev. Lett.*, 2019, **122**, 063603.
- 36 J. F. Triana and J. L. Sanz-Vicario, *J. Chem. Phys.*, 2021, **154**, 094120.
- 37 J. F. Triana and F. Herrera, *New J. Phys.*, 2022, **24**, 023008.
- 38 R. Borrego-Varillas, M. Lucchini, T. Schnappinger, M. Murari, G. D. Lucarelli, F. Daniele, F. Frassetto, L. Poletto, R. de Vivie-Riedle and M. Nisoli, Few-femtosecond dynamics of CO₂ super-excited states, Proceedings of the OSA 22nd International Conference on Ultrafast Phenomena, Virtual event, China, 2020.